





Communication

# Green Synthesis of $\text{Ge}_{1-x}\text{Sn}_x$ Alloy Nanoparticles for Optoelectronic Applications

Gopal Singh Attar , Mimi Liu , Cheng-Yu Lai  and Daniela R. Radu \* 

Department of Mechanical and Materials Engineering, Florida International University, Miami, FL 33174, USA; gattar@fiu.edu (G.S.A.); mliu@fiu.edu (M.L.); clai@fiu.edu (C.-Y.L.)

\* Correspondence: dradu@fiu.edu

**Abstract:** Compositionally controlled, light-emitting, group IV semiconductor nanomaterials have potential to enable on-chip data communications and infrared (IR) imaging devices compatible with the complementary metal–oxide–semiconductor (CMOS) technology. The recent demonstration of a direct band gap laser in Ge–Sn alloys opens avenues to the expansion of Si-photonics. Ge–Sn alloys showed improved effective carrier mobility as well as direct band gap behavior at Sn composition above 6–11%. In this work,  $\text{Ge}_{1-x}\text{Sn}_x$  alloy nanoparticles with varying Sn compositions from  $x = 0.124$  to  $0.178$  were prepared via colloidal synthesis using sodium borohydride ( $\text{NaBH}_4$ ), a mild and non-hazardous reducing reagent. Successful removal of the synthesized long-alkyl-chain ligands present on nanoparticles' surfaces, along with the passivation of the Ge–Sn nanoparticle surface, was achieved using aqueous  $(\text{NH}_4)_2\text{S}$ . The highly reactive surface of the nanoparticles prior to ligand exchange often leads to the formation of germanium oxide ( $\text{GeO}_2$ ). This work demonstrates that the  $(\text{NH}_4)_2\text{S}$  further acts as an etching reagent to remove the oxide layer from the particles' surfaces. The compositional control and long-term stability will enable the future use of these easily prepared  $\text{Ge}_{1-x}\text{Sn}_x$  nanoalloys in optoelectronic devices.



**Citation:** Attar, G.S.; Liu, M.; Lai, C.-Y.; Radu, D.R. Green Synthesis of  $\text{Ge}_{1-x}\text{Sn}_x$  Alloy Nanoparticles for Optoelectronic Applications. *Crystals* **2021**, *11*, 1216. <https://doi.org/10.3390/cryst11101216>

Academic Editor: Dmitri Donetski

Received: 18 September 2021

Accepted: 5 October 2021

Published: 8 October 2021

**Publisher's Note:** MDPI stays neutral with regard to jurisdictional claims in published maps and institutional affiliations.



**Copyright:** © 2021 by the authors. Licensee MDPI, Basel, Switzerland. This article is an open access article distributed under the terms and conditions of the Creative Commons Attribution (CC BY) license (<https://creativecommons.org/licenses/by/4.0/>).

**Keywords:** germanium-tin alloy; colloidal synthesis; nanoparticles; electronic materials; semiconductors

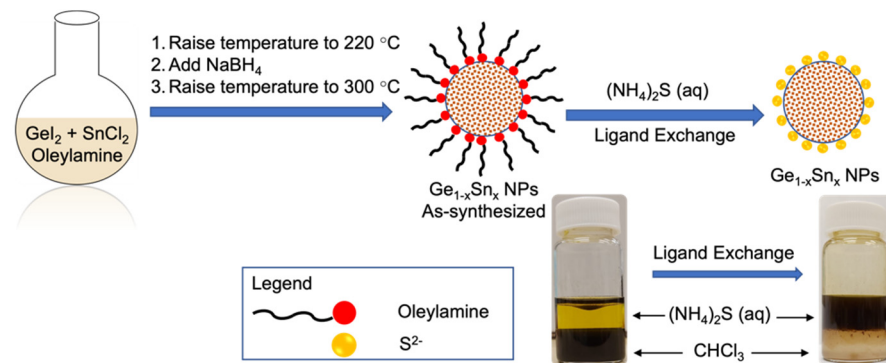
## 1. Introduction

Germanium-tin (Ge–Sn) is a complementary metal–oxide–semiconductor (CMOS) compatible group IV semiconductor material that has attracted great attention over the past two decades owing to its compatibility with Si and its great potential for use in optoelectronic integration circuits (OEIC) [1]. When the Sn content exceeds  $x = 0.06$ – $0.11$ , the material becomes a direct bandgap semiconductor, offering a paradigm shift for Si-photonics toward the monolithic integration of light emitters [2,3]. The favorable optical properties originate in a modified band structure, changing the bandgap from an indirect to a direct one. The first demonstration of such a direct band gap laser has recently been accomplished for Ge–Sn [2]. Ge–Sn has been also reported to have a higher effective hole mobility than Ge due to the decrease in light hole effective mass of Ge–Sn, with the incorporation of Sn in the case of p-channel metal–oxide–semiconductor field effect transistors (p-MOSFETs) [4]. The bandgap of  $\text{Ge}_{1-x}\text{Sn}_x$  can be tuned from 0.6 to 0 eV by varying the Sn content, thus making this alloy suitable for use in near-infrared and mid-infrared detectors [3].

However, the high crystallization temperature of Ge (above  $300\text{ }^\circ\text{C}$ ) and large lattice mismatch ( $\sim 14\%$ ) with Sn, as well as the low equilibrium solubility ( $<1\%$ ) of Sn in Ge, make it difficult to synthesize compositionally uniform  $\text{Ge}_{1-x}\text{Sn}_x$  alloys [5]. Recently, various Ge–Sn materials, including alloy nanocrystals [6], quantum dots [7], nanowires [8], and core/shell particles [9] have been reported. Different strategies such as pulsed laser melting [10], epitaxial growth [11], microwave synthesis [12] and solution-based methods [13] have been investigated to produce direct gap group IV semiconductors. Of all

the strategies, colloidal synthesis of high-quality  $\text{Ge}_{1-x}\text{Sn}_x$  without phase segregation of Sn is a desirable route that would enable inexpensive fabrication, processing, and device assembly [14].

In this work, we report the colloidal synthesis, characterization, and physical properties of a series of  $\text{Ge}_{1-x}\text{Sn}_x$  alloy nanoparticles with Sn compositions ranging from  $x = 0.124$  to  $0.178$ , which resulted from the intended doping concentrations of  $x = 0.12, 0.15, 0.18$ . This range of concentrations was selected to obtain the direct band gap semiconductor behavior for the  $\text{Ge}_{1-x}\text{Sn}_x$  alloy, provided that the transition from an indirect to direct band gap occurred when the doping concentration of Sn exceeded  $x = 0.06\text{--}0.11$ . We were able to obtain  $\text{Ge}_{1-x}\text{Sn}_x$  nanoparticles with  $x = 0.124, 0.151$  and  $0.178$ . For doping concentrations exceeding  $x = 0.20$ , we observed the segregation of Sn. The nanoparticles were obtained by using  $\text{NaBH}_4$  as a reducing agent, which is mild, safer to use and easier to handle than stronger, more highly reactive and pyrophoric agents such as *n*-BuLi and  $\text{LiAlH}_4$ . Oleylamine surface ligands that remained on the particle's surface upon synthesis were exchanged with short sulfide ligands by a solution-phase ligand-exchange approach using aqueous  $(\text{NH}_4)_2\text{S}$  [15]. It was found that the  $(\text{NH}_4)_2\text{S}$  not only effectively passivated the surface of Ge-Sn from oxidation but the process also successfully removed the undesired surface oxides. The synthesis and ligand exchange processes are shown in Scheme 1.



**Scheme 1.** An illustration of the synthesis and ligand exchange process of  $\text{Ge}_{1-x}\text{Sn}_x$  alloy nanoparticles.

## 2. Materials and Methods

### 2.1. Materials

Tin dichloride (98%) was purchased from Sigma Aldrich (Saint Louis, MO, USA) and germanium diiodide was purchased from Gelest Inc. (Morrisville, PA, USA) and stored under argon. Oleylamine (70%) and sodium borohydride ( $\text{NaBH}_4$ ) solution (2.0 M in triethyleneglycol dimethyl ether) were purchased from Sigma Aldrich (Saint Louis, MO, USA). ACS-grade solvents, methanol, chloroform, and toluene, were purchased from Fisher Scientific (Waltham, MA, USA) and used without further purification.  $(\text{NH}_4)_2\text{S}$  (20% solution in water diluted to 10% before use) was purchased from Fisher Scientific (Waltham, MA, USA). OLA was dried by heating at  $120\text{ }^\circ\text{C}$  under vacuum for 1 h prior to storage under argon.

### 2.2. Characterization

The crystal structure and purity of the prepared alloy nanoparticles were determined by X-ray powder diffraction (XRD) using a Rigaku Miniflex 600 X-Ray diffractometer (Tokyo, Japan) ( $\text{Cu K}\alpha$  radiation,  $\lambda = 1.5405\text{ \AA}$ ). Crystallite sizes were estimated by applying the Scherrer formula to the (111), (220), and (311) reflections of cubic Ge. To confirm product purity by Raman spectroscopy, Raman spectra were obtained with a WITec Alpha 300 Raman microscope (Ulm, (Bavaria), Germany) equipped with a 532 nm laser. The morphology and size of the synthesized alloy nanoparticles were determined by transmission electron microscopy (TEM) imaging, using a Talos F200X (FEI, Hillsboro, OR, USA), and scanning electron microscopy (SEM) imaging, with a JEOL 6330F (Peabody,

MA, USA). Elemental distribution of the alloy nanoparticles was determined with the energy dispersive spectroscopy (EDS) feature of the JEOL 6330F SEM and Talos F200X TEM. The nanoparticles absorption spectra were collected using a Shimadzu UV-3600 Plus Ultraviolet–Visible–Near-Infrared (UV–Vis–NIR) spectrophotometer (Shimadzu, Kyoto, Japan).

### 2.3. Preparation of Ge–Sn Nanoparticles

An amount of 10 mL of oleylamine was added to a 100 mL two-necked round-bottomed flask and degassed at 120 °C for at least 1 hour. After cooling to room temperature, it was flushed with argon and the flask was transferred to the glovebox. Predetermined amounts of GeI<sub>2</sub> and SnCl<sub>2</sub> for each experimental setting (Table 1) were added to the flask and the entire setup was sealed and carefully transferred to the Schlenk line.

The reaction mixture was further degassed at 120 °C and flushed with argon. The process was repeated three times. The temperature was raised to 220 °C and 0.5 mL of NaBH<sub>4</sub> (2.0 M in triethyleneglycol dimethylether) was added. The color of the reaction mixture immediately turned brown upon NaBH<sub>4</sub> addition. The reaction temperature was further raised to 300 °C and kept at this temperature for 60 min followed by cooling of the reaction mixture with compressed air.

**Table 1.** Amounts of GeI<sub>2</sub> and SnCl<sub>2</sub> for the synthesis of Ge<sub>1–x</sub>Sn<sub>x</sub> nanoparticles.

Targeted Composition	GeI <sub>2</sub> Amount		SnCl <sub>2</sub> Amount	
	mg	mmol	mg	mmol
Ge <sub>0.88</sub> Sn <sub>0.12</sub>	172.3	0.528	13.6	0.072
Ge <sub>0.85</sub> Sn <sub>0.15</sub>	166.5	0.510	17.1	0.090
Ge <sub>0.82</sub> Sn <sub>0.18</sub>	160.6	0.492	20.5	0.108

After cooling to room temperature, 10 mL of toluene and 70 mL of methanol were added to the flask to precipitate the nanoparticles. The mixture was transferred to a 50 mL centrifuge tube and centrifuged at 8000 rpm for 10 min to obtain the Ge–Sn alloy nanoparticles. The supernatant was discarded and the solid product—a black color pellet—was further dispersed in 10 mL toluene and reprecipitated by adding 30 mL methanol. This process was repeated twice. The final product was collected by centrifugation and dried in a vacuum oven.

### 2.4. Ligand Exchange and Surface Oxide Removal

A suspension (5 mL) of Ge–Sn nanoparticles in chloroform (5 mg/mL) was mixed with 5 mL of aqueous (NH<sub>4</sub>)<sub>2</sub>S solution (10%) in a vial. The mixture was shaken vigorously for 2 min and allowed to settle until the chloroform and aqueous (NH<sub>4</sub>)<sub>2</sub>S were phase-separated. The Ge–Sn nanoparticles completely transferred from the chloroform phase to the aqueous (NH<sub>4</sub>)<sub>2</sub>S phase. An amount of 10 mL ethanol was added to the vial, and the mixture was transferred to a centrifuge tube and centrifuged for 4 min at 6000 RPM. The supernatant was discarded, and the precipitate was washed with a mixture of ethanol: chloroform (1:1, 20 mL) twice. The product collected after centrifugation was dried overnight in vacuum oven for further use.

## 3. Results and Discussion

### 3.1. Synthesis

Phase-pure Ge<sub>1–x</sub>Sn<sub>x</sub> nanoparticles with compositions in the range of  $x = 0.124–0.178$  were successfully produced by the co-reduction of GeI<sub>2</sub> and SnCl<sub>2</sub>. The synthesized nanoparticles were found to be very stable even for months after synthesis. No sign of degradation or surface oxidation was observed even three months after the synthesis while stored under ambient conditions (Figure S1, Supplementary Materials). Reactions with higher Sn/Ge ratios produced the alloy nanoparticles with a lower percentage of Sn incorporation along with the formation of  $\beta$ -Sn impurities (Figure S2, Supplementary Materials).

All of these reactions were very sensitive and a rigorous approach is required to exclude even traces of moisture and air from the system. Even after taking caution, minor peaks of  $\text{GeO}_2$  were observed due to exposure to air during workup under ambient conditions.

### 3.2. XRD and Raman Analysis

With an increasing Sn concentration, the powder X-ray diffraction (XRD) patterns shift to lower  $2\theta$  angles owing to the expansion of the cubic Ge structure by  $\alpha$ -Sn, suggesting the incorporation of Sn into Ge (Vegard's Law) [16]. The major diffraction peaks were indexed to the (111), (220), and (311) planes of diamond-cubic Ge with  $F\bar{3}m$  space group (ICDD: 01-080-6669). No diffraction peaks corresponding to  $\alpha$ -Sn, or  $\beta$ -Sn (tetragonal Sn) impurity phases were detected. The peak observed near  $26^\circ 2\theta$ , attributable to  $\text{GeO}_2$  (Figure 1a) could be ascribed to ambient isolation and purification of nanoparticles, as weakly bound surfactant ligands can be lost via excessive washing and centrifugation, thus exposing the nanoparticles surface [17]. The lattice constants for cubic Ge and  $\alpha$ -Sn are 5.66 and 6.49 Å, respectively. In contrast, the lattice constant values in  $\text{Ge}_{1-x}\text{Sn}_x$  nanoparticles vary from 5.76 Å for  $x = 0.124$  to 5.794 Å for  $x = 0.178$  (Table S1, Supplementary Materials). The values of lattice constants indicate a near linear expansion of the cubic Ge structure with increasing Sn. This experimentally observed trend of increasing lattice constant values was found to be in agreement with Vegard's rule (Figure 1b) [16], which states that the lattice parameter of the alloys varies linearly with the change in the concentration of the components.

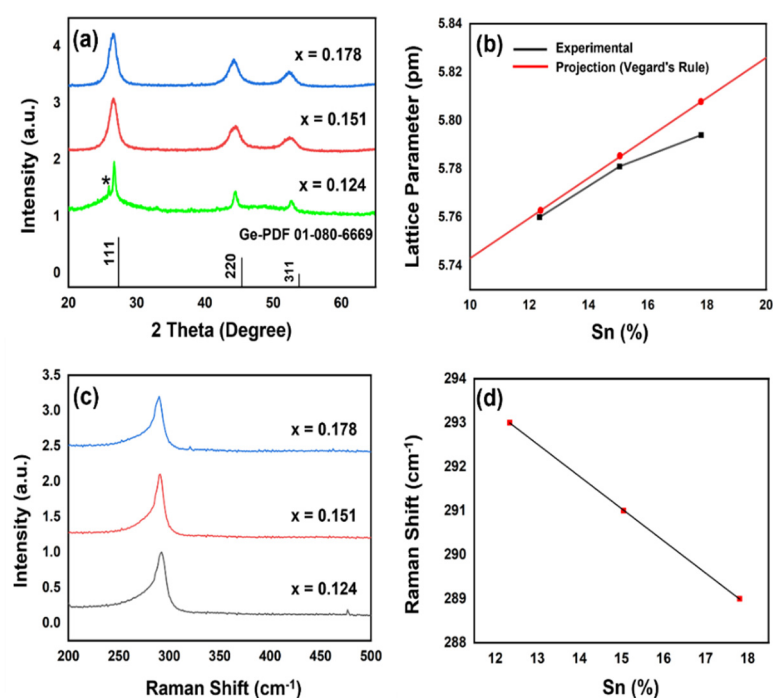


**Figure 1.** (a) Powder XRD patterns of  $\text{Ge}_{1-x}\text{Sn}_x$  nanoparticles. (b) A plot illustrating the lattice parameters based on XRD patterns (Black) and projection of theoretical lattice parameters calculated using Vegard's law (Red). \*  $\text{GeO}_2$  impurity peak. (c) Raman spectra of the  $\text{Ge}_{1-x}\text{Sn}_x$  nanoparticles. (d) A plot illustrating the systematic red-shifting of the Ge–Ge optical phonon mode with increasing Sn composition.

Bulk Ge exhibits a Raman peak at  $300 \text{ cm}^{-1}$  that corresponds to the longitudinal optical (LO) phonon mode of Ge–Ge bonds [18]. As heavier Sn atoms are incorporated into the Ge crystal, a systematic red shift of the Ge–Ge phonon mode ( $288\text{--}282 \text{ cm}^{-1}$  for  $x = 0.124\text{--}0.178$ ) was observed as a result of the longer Ge–Sn bonds and the heavier Sn atoms [19]. The observed red shift with increasing Sn content is consistent with the

weakening (or lengthening) of the Ge–Ge bond and lattice constants computed from Vegard’s law (Figure 1c).

### 3.3. SEM and TEM

In conjunction with the XRD and Raman analysis, SEM and TEM have been used to confirm the formation, compositional uniformity, and homogeneity of Ge–Sn nanoparticles. The TEM image shows that the as-synthesized nanoparticles are irregular in shape and polydisperse (Figure 2a). The high-resolution TEM image (HRTEM) indicates the lattice spacing of 3.3 Å, which corresponds to the expanded (111) plane of diamond cubic  $\text{Ge}_{1-x}\text{Sn}_x$  and is slightly larger than that of pure Ge (3.26 Å) [20], further confirming the expansion of cubic Ge lattice (Figure 2b). The TEM-EDS and SEM-EDS elemental mapping profile shows that the Sn and Ge are uniformly distributed over the entire nanoparticle, confirming it as a homogeneous, solid solution and free of segregated Sn species. EDX data of  $\text{Ge}_{1-x}\text{Sn}_x$  nanocrystals show good agreement with the elemental composition calculated by Vegard’s law.

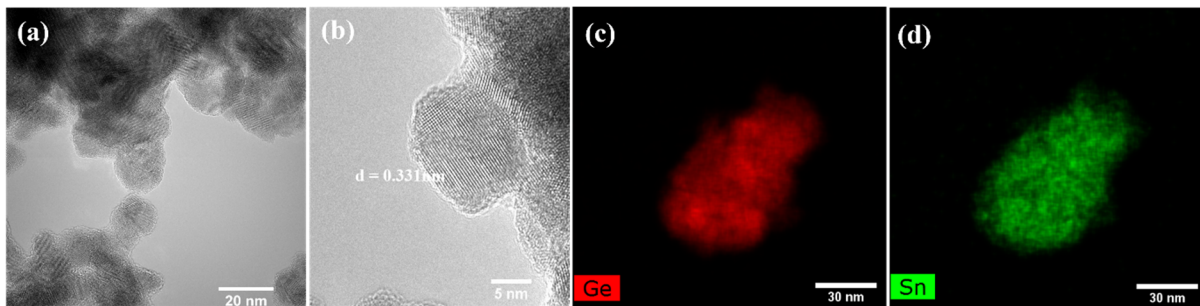


**Figure 2.** (a) HRTEM images of  $\text{Ge}_{1-x}\text{Sn}_x$  nanoparticles ( $x = 0.151$ ). (b) HRTEM image of  $\text{Ge}_{1-x}\text{Sn}_x$  nanoparticles ( $x = 0.151$ ), showing lattice fringes that correspond to the (111) plane of cubic Ge. (c) and (d) TEM/EDS elemental maps of Ge and Sn, respectively.

### 3.4. Optical Properties and Ligand Exchange

The solution-based UV–Vis–NIR spectra of the samples dispersed in chloroform was featureless across the whole range of wavelengths (Figure 3a). The incorporation of Sn significantly red-shifts the absorption onsets into the near-IR (NIR) region, further expanding its optical window for application in NIR optoelectronic devices.

The as-synthesized nanoparticles carry surface ligands originated from the synthesis. Various methods for replacing the long-alkyl-chain solvent/stabilizer used in synthesis have been reported [15,21–24]. Such methods include the replacement of oleylamine with much shorter atomic  $\text{S}^{2-}$  ligands by a solution-phase ligand-exchange process, accomplished by vigorously shaking a mixture of nanoparticles suspended in an adequate solvent (chloroform used herein) and aqueous  $(\text{NH}_4)_2\text{S}$ . The removal of the surface ligands was qualitatively validated by the loss of nanoparticle dispersibility in chloroform and further confirmed by FT-IR analysis, which shows the disappearance of bands centered around  $2800\text{--}3000\text{ cm}^{-1}$  ascribed to C–H stretching vibrations of oleylamine (Figure 3b). The XRD pattern of the sample in Figure 3c confirms the phase purity of  $\text{Ge}_{1-x}\text{Sn}_x$  nanoparticles after the ligand exchange. According to the literature,  $(\text{NH}_4)_2\text{S}$  treatment creates a  $\text{Ge}_{1-x}\text{Sn}_x\text{--S}$  monolayer passivating the dangling surface bonds of both Ge and Sn, and thus protects  $\text{Ge}_{1-x}\text{Sn}_x$  surfaces from oxidation [25].



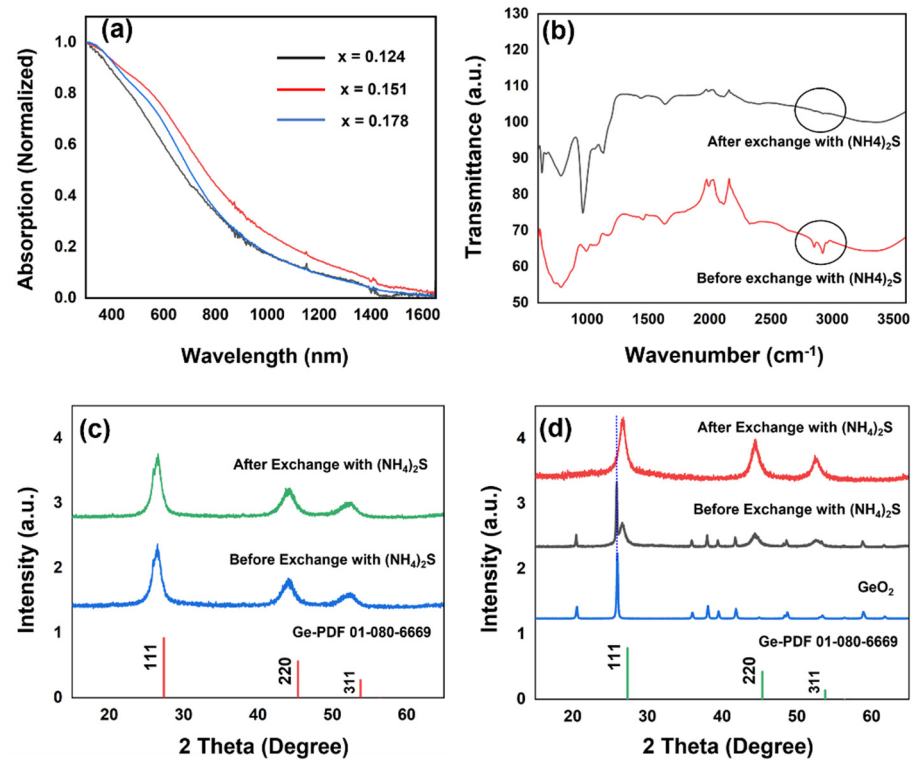


**Figure 3.** (a) UV–Vis spectrum of the prepared  $\text{Ge}_{1-x}\text{Sn}_x$  nanoparticles. (b) FT-IR spectra of  $\text{Ge}_{1-x}\text{Sn}_x$  nanoparticles sample before and after ligand exchange. (c) and (d) Powder XRD patterns of  $\text{Ge}_{1-x}\text{Sn}_x$  nanoparticles sample before and after ligand exchange.

The treatment with aqueous  $(\text{NH}_4)_2\text{S}$  not only successfully exchanged the surface ligands but also removed the native surface oxide, which could cause poor chemical stability, high surface trap state density, and unfavorable electrical properties. The powder XRD analysis of  $\text{Ge}_{1-x}\text{Sn}_x$  samples containing the  $\text{GeO}_2$  impurity shows the complete elimination of the corresponding oxide peaks after treatment with aqueous  $(\text{NH}_4)_2\text{S}$  (Figure 3d). It is anticipated that the removal of oxide impurities from the surface of  $\text{Ge}_{1-x}\text{Sn}_x$  alloy nanoparticles will further improve their charge, career mobility and performance in electronic devices.

#### 4. Conclusions

The successful synthesis of uniform  $\text{Ge}_{1-x}\text{Sn}_x$  alloy nanoparticles with Sn concentrations varying from  $x = 0.124$  to  $0.178$  using the mild reducing reagent  $\text{NaBH}_4$  has been achieved, proving to be a facile, ecofriendly, and economically viable route for producing Ge-Sn nanoparticles. Using a solution-phase ligand-exchange approach, the long-chain oleylamine ligands were replaced by short inorganic sulfide-capping groups using aqueous  $(\text{NH}_4)_2\text{S}$ . The surface-passivating effect of  $(\text{NH}_4)_2\text{S}$  suppresses the formation of germanium oxide while preventing any segregation of Sn atoms, as showed by the long-term stability of the nanomaterial.  $(\text{NH}_4)_2\text{S}$  not only successfully removes the organic ligands but also etches any undesired surface oxide that occasionally forms during synthesis.

**Supplementary Materials:** The following are available online at <https://www.mdpi.com/article/10.3390/cryst11101216/s1>, Table S1: Crystallite size and lattice parameter of  $\text{Ge}_{1-x}\text{Sn}_x$  alloy nanoparticles, Figure S1: Powder XRD patterns of  $\text{Ge}_{1-x}\text{Sn}_x$  nanoparticles after months of storage under ambient conditions, Figure S2: Powder XRD patterns of  $\text{Ge}_{1-x}\text{Sn}_x$  nanoparticles with higher composition of Sn (20–30%) showing peaks of segregated Sn impurities, Figure S3: (a–c) SEM images of  $\text{Ge}_{1-x}\text{Sn}_x$  nanoparticles ( $x = 0.15$ ). (d,e) Ge and Sn SEM–EDX element mapping from the image c, showing that Ge and Sn are homogeneously dispersed through the alloy nanoparticles, Figure S4: (a–c) SEM images of  $\text{Ge}_{1-x}\text{Sn}_x$  nanoparticles ( $x = 0.178$ ). (d,e) Ge and Sn SEM–EDX element

mapping from the image c, showing that Ge and Sn are homogeneously dispersed through the alloy nanoparticles, Figure S5: Representative SEM-EDS spectrum of  $\text{Ge}_{0.85}\text{Sn}_{0.15}$  nanoparticles.

**Author Contributions:** The individual authors' contributions are as follows: conceptualization of the synthetic pathway, D.R.R. and C.-Y.L.; methodology for the synthetic approach, G.S.A. and M.L.; validation of data and processes, D.R.R. and C.-Y.L.; formal analysis of the research results, G.S.A.; investigation, G.S.A. and M.L.; resources provided for the project, D.R.R. and C.-Y.L.; data curation, G.S.A.; writing—original draft preparation, G.S.A.; writing—review and editing, D.R.R. and C.-Y.L.; supervision, D.R.R. and C.-Y.L.; project administration, D.R.R. and C.-Y.L.; funding acquisition, D.R.R. and C.-Y.L. All authors have read and agreed to the published version of the manuscript.

**Funding:** This research was funded by the US Department of Defense, Office of Naval Research (ONR), Award number N00014-20-1-2539, the US National Aeronautics and Space Administration (NASA) Award number 80NSSC10M0201, and the US National Science Foundation, Award number NSF1924412.

**Institutional Review Board Statement:** Not applicable.

**Informed Consent Statement:** Not applicable.

**Data Availability Statement:** Data and methods used in this work are presented in sufficient detail in the paper so that other researchers can replicate the work. Raw data are available from the corresponding author upon request.

**Conflicts of Interest:** The authors declare no conflict of interest. The funders had no role in the design of the study; in the collection, analyses, or interpretation of data; in the writing of the manuscript, or in the decision to publish the results.

## References

- Ruddy, D.; Johnson, J.; Smith, E.R.; Neale, N. Size and Bandgap Control in the Solution-Phase Synthesis of Near-Infrared-Emitting Germanium Nanocrystals. *ACS Nano* **2010**, *4*, 7459–7466. [[CrossRef](#)] [[PubMed](#)]
- Geiger, R.; Zabel, T.; Sigg, H. Group IV Direct Band Gap Photonics: Methods, Challenges, and Opportunities. *Front. Mater.* **2015**, *2*, 52. [[CrossRef](#)]
- Suyog, G.; Chen, R.; Huang, Y.-C.; Yihwan, K.; Sanchez, E.; Harris, J.S.; Saraswat, K.C. Highly Selective Dry Etching of Germanium over Germanium–Tin ( $\text{Ge}_{1-x}\text{Sn}_x$ ): A Novel Route for  $\text{Ge}_{1-x}\text{Sn}_x$  Nanostructure Fabrication. *Nano Lett.* **2013**, *13*, 3783–3790.
- Wang, L.; Su, S.; Wang, W.; Gong, X.; Yang, Y.; Guo, P.; Zhang, G.; Xue, C.; Cheng, B.; Han, G.; et al. Strained germanium–tin ( $\text{GeSn}$ ) p-channel metal-oxide-semiconductor field-effect-transistors (p-MOSFETs) with ammonium sulfide passivation. *Solid-State Electron.* **2013**, *83*, 66–70. [[CrossRef](#)]
- Kittel, C. *Introduction to Solid State Physics*; John Wiley & Sons Inc.: New York, NY, USA, 2005.
- Esteves, R.J.A.; Hafiz, S.; Demchenko, D.O.; Özgür, Ü.; Arachchige, I.U. Ultra-Small  $\text{Ge}_{1-x}\text{Sn}_x$  Quantum Dots with Visible Photoluminescence. *Chem. Commun.* **2016**, *52*, 11665–11668. [[CrossRef](#)]
- Venkatesham, T.; Nakagawara, T.A.; Demchenko, D.O.; Özgür, Ü.; Arachchige, I.U.  $\text{Ge}_{1-x}\text{Sn}_x$  Alloy Quantum Dots with Composition-Tunable Energy Gaps and near-Infrared Photoluminescence. *Nanoscale* **2018**, *10*, 20296–20305.
- Barth, S.; Seifner, M.S.; Bernardi, J. Microwave-Assisted Solution–Liquid–Solid Growth of  $\text{Ge}_{1-x}\text{Sn}_x$  Nanowires with High Tin Content. *Chem. Commun.* **2015**, *51*, 12282–12285. [[CrossRef](#)]
- Meng, A.C.; Fenrich, C.; Braun, M.; McVittie, J.P.; Marshall, A.F.; Harris, J.S.; McIntyre, P.C. Core-Shell Germanium/Germanium–Tin Nanowires Exhibiting Room-Temperature Direct- and Indirect-Gap Photoluminescence. *Nano Lett.* **2016**, *16*, 7521–7529. [[CrossRef](#)]
- Gao, K.; Prucnal, S.; Huebner, R.; Baetz, C.; Skorupa, I.; Wang, Y.; Helm, M.; Zhou, S.; Skorupa, W.  $\text{Ge}_{1-x}\text{Sn}_x$  alloys synthesized by ion implantation and pulsed laser melting. *Appl. Phys. Lett.* **2014**, *105*, 42107. [[CrossRef](#)]
- Kormoš, L.; Kratzer, M.; Kosteci, K.; Oehme, M.; Šikola, T.; Kasper, E.; Schulze, J.; Teichert, C. Surface analysis of epitaxially grown  $\text{GeSn}$  alloys with Sn contents between 15% and 18%. *Surf. Interface Anal.* **2016**, *49*, 297–302. [[CrossRef](#)]
- Newton, K.A.; Sully, H.R.; Bridges, F.; Carter, S.A.; Kauzlarich, S.M. Structural Characterization of Oleylamine- and Dodecanethiol-Capped  $\text{Ge}_{1-x}\text{Sn}_x$  Alloy Nanocrystals. *J. Phys. Chem. C* **2021**, *125*, 6401–6417. [[CrossRef](#)]
- Lu, X.; Korgel, A.B.A.; Johnston, K.P. High Yield of Germanium Nanocrystals Synthesized from Germanium Diodide in Solution. *Chem. Mater.* **2005**, *17*, 6479–6485. [[CrossRef](#)]
- Esteves, R.J.A.; Ho, M.Q.; Arachchige, I.U. Nanocrystalline Group IV Alloy Semiconductors: Synthesis and Characterization of  $\text{Ge}_{1-x}\text{Sn}_x$  Quantum Dots for Tunable Bandgaps. *Chem. Mater.* **2015**, *27*, 1559–1568. [[CrossRef](#)]
- Nag, A.; Kovalenko, M.V.; Lee, J.-S.; Liu, W.; Spokoyny, B.; Talapin, D.V. Metal-Free Inorganic Ligands for Colloidal Nanocrystals:  $\text{S}^{2-}$ ,  $\text{HS}^-$ ,  $\text{Se}^{2-}$ ,  $\text{HSe}^-$ ,  $\text{Te}^{2-}$ ,  $\text{HTe}^-$ ,  $\text{TeS}_3^{2-}$ ,  $\text{OH}^-$ , and  $\text{NH}_2^-$  as Surface Ligands. *J. Am. Chem. Soc.* **2011**, *133*, 10612–10620. [[CrossRef](#)]
- Chizmeshya, A.V.G.; Bauer, M.R.; Kouvetakis, J. Experimental and Theoretical Study of Deviations from Vegard's Law in the  $\text{Sn}_x\text{Ge}_{1-x}$  System. *ChemInform* **2003**, *34*. [[CrossRef](#)]

17. Lee, D.C.; Pietryga, J.M.; Robel, I.; Werder, D.J.; Schaller, R.D.; Klimov, V. Colloidal Synthesis of Infrared-Emitting Germanium Nanocrystals. *J. Am. Chem. Soc.* **2009**, *131*, 3436–3437. [[CrossRef](#)] [[PubMed](#)]
18. Volodin, V.A.; Marin, D.; Sachkov, V.; Gorokhov, E.B.; Rinnert, H.; Vergnat, M. Applying an improved phonon confinement model to the analysis of Raman spectra of germanium nanocrystals. *J. Exp. Theor. Phys.* **2014**, *118*, 65–71. [[CrossRef](#)]
19. Boote, B.W.; Men, L.; Andaraarachchi, H.P.; Bhattacharjee, U.; Petrich, J.W.; Vela, J.; Smith, E.A. Germanium–Tin/Cadmium Sulfide Core/Shell Nanocrystals with Enhanced Near-Infrared Photoluminescence. *Chem. Mater.* **2017**, *29*, 6012–6021. [[CrossRef](#)]
20. Yang, Q.; Zhao, X.; Wu, X.; Li, M.; Di, Q.; Fan, X.; Zhu, J.; Song, X.; Li, Q.; Quan, Z. Facile Synthesis of Uniform  $\text{Ge}_{1-x}\text{Sn}_x$  Alloy Nanocrystals with Tunable Bandgap. *Chem. Mater.* **2019**, *31*, 2248–2252. [[CrossRef](#)]
21. Chen, C.-C.; Stone, K.; Lai, C.-Y.; Dobson, K.; Radu, D. Sulvanite ( $\text{Cu}_3\text{VS}_4$ ) nanocrystals for printable thin film photovoltaics. *Mater. Lett.* **2018**, *211*, 179–182. [[CrossRef](#)]
22. Liu, M.; Lai, C.-Y.; Chang, C.-Y.; Radu, D.R. Solution-Based Synthesis of Sulvanite  $\text{Cu}_3\text{TaS}_4$  and  $\text{Cu}_3\text{TaSe}_4$  Nanocrystals. *Crystals* **2021**, *11*, 51. [[CrossRef](#)]
23. Liu, M.; Lai, C.-Y.; Selopal, G.S.; Radu, D.R. Synthesis and optoelectronic properties of  $\text{Cu}_3\text{VSe}_4$  nanocrystals. *PLoS ONE* **2020**, *15*, e0232184. [[CrossRef](#)] [[PubMed](#)]
24. Liu, M.; Radu, D.; Selopal, G.; Bachu, S.; Lai, C.-Y. Stand-Alone  $\text{CuFeSe}_2$  (Eskebornite) Nanosheets for Photothermal Cancer Therapy. *Nanomaterials* **2021**, *11*, 2008. [[CrossRef](#)] [[PubMed](#)]
25. Lei, D.; Wang, W.; Zhang, Z.; Pan, J.; Gong, X.; Liang, G.; Tok, E.-S.; Yeo, Y.-C.  $\text{Ge}_{0.83}\text{Sn}_{0.17}$  p-channel metal-oxide-semiconductor field-effect transistors: Impact of sulfur passivation on gate stack quality. *J. Appl. Phys.* **2016**, *119*, 24502. [[CrossRef](#)]